nature energy
REVIEW ARTICLE
https://doi.org/10.1038/s41560-017-0016-9

Emergence of highly transparent photovoltaics for distributed applications

Christopher J. Traverse[1], Richa Pandey[2], Miles C. Barr[2] and Richard R. Lunt[1,3]*

Solar energy offers a viable solution to our growing energy need. While adoption of conventional photovoltaics on rooftops and in solar farms has grown rapidly in the last decade, there is still plenty of opportunity for expansion. See-through solar technologies with partial light transmission developed over the past 30 years have initiated methods of integration not possible with conventional modules. The large-scale deployment necessary to offset global energy consumption could be further accelerated by developing fully invisible solar cells that selectively absorb ultraviolet and near-infrared light, allowing many of the surfaces of our built environment to be turned into solar harvesting arrays without impacting the function or aesthetics. Here, we review recent advances in photovoltaics with varying degrees of visible light transparency. We discuss the figures of merit necessary to characterize transparent photovoltaics, and outline the requirements to enable their widespread adoption in buildings, windows, electronic device displays, and automobiles.

Moving global energy consumption away from fossil fuels requires innovative and cost-effective renewable energy technologies. Photovoltaics (PV) can fulfil this need many times over if deployed over a large enough area. For example, a theoretical solar installation covering approximately 20% of Nevada could power the United States[1]. However, the current installed area of terrestrial PV technologies only provides approximately 1% of the worldwide energy demand[2,3]. While the potential of theoretical large-area PV installations in remote and sunny regions can meet this demand, maintenance and distribution costs as well as adverse environmental effects make this less practical[2].

One approach to aid in this large-scale demand is through the development of building-integrated PV (BIPV) and building-applied PV (BAPV) to generate electricity close to where it is utilized during peak demand, which can reduce electrical transmission losses, the need for storage capacity, and installation costs. BIPV are integrated directly into facades or other areas of buildings as replacements for conventional building materials while BAPV are modules retrofitted onto areas such as rooftops (Fig. 1a) or awnings after initial construction. In addition to generating power, BIPV and BAPV can serve secondary purposes such as providing shade[4]. New BIPV technologies are being intimately integrated into the architectures of buildings around the world but have only modestly contributed to offset their energy consumption so far[5]. Considerably larger installation areas are required to achieve significant energy offset.

The total amount of rooftop area in the United States suitable for conventional PV installation[6] is greater than 8 billion m^2. Assuming a module power efficiency of 16%, the total potential of rooftop-mounted PV is conservatively estimated as 1400 TWh yr^{-1} (0.16TW), or nearly 40% of the total electricity generation of the United States. While this rooftop potential is substantial, the additional surface area around buildings (siding, windows, and so on) is vastly underutilized and offers a tremendous opportunity to more than double the rooftop harvesting area[7,8] and help achieve net zero energy consumption. Transparent PV (TPV), which optimize both average visible transmission (AVT, see Box 1) and power conversion efficiency (PCE), can tap this area without impacting underlying facades and windows (Fig. 1b–f).

TPV technologies are grouped into variants that are either wavelength-selective or non-wavelength-selective in their absorption of visible light. Non-wavelength-selective technologies produce electricity from broad absorption of the solar spectrum (including visible photons) and achieve some AVT by either segmenting opaque PV cells (Fig. 1b) or using a sufficiently thin or low-concentration photoactive material (Fig. 1c,d). These non-wavelength-selective TPV technologies typically exhibit AVT values between 0–50% and are important in applications such as tinted windows and decorative construction exteriors[9,10]. Wavelength-selective TPV employ photoactive materials that preferentially harvest ultraviolet (UV) and near-infrared (NIR) light, while selectively transmitting the visible spectrum (Fig. 1e,f) and have generally demonstrated AVT values of 50–90%.

Here, we discuss the development and performance limits of TPV technologies, including transparent solar cells, luminescent solar concentrators (LSC) and scattering solar concentrators. We detail both established and new figures of merit that determine the integration requirements for various applications and summarize the challenges to be addressed for wide-scale deployment, while showing that wavelength-selective TPV can exhibit performances nearly comparable to opaque cells and non-wavelength-selective cells. With a large potential for additional installed surface area, TPV could become instrumental in offsetting worldwide energy demand by enabling new routes for solar deployment that complement conventional module installations.

Theoretical potential limits of TPV

By selectively harvesting UV (<435 nm) and NIR (>670 nm) wavelengths (Fig. 2a,b), the theoretical Shockley–Queisser (SQ) limit for the PCE of a wavelength-selective TPV single junction with 100% AVT is 20.6%, compared to 33.1% for an opaque PV[10]. The optimal bandgap is redshifted from 1.36 eV (910 nm) to 1.12 eV (1,100 nm) in going from opaque to visibly transparent cells due to the balance in absorption and voltage given the transmission of visible light. This efficiency limit for selective TPV stems from the large fraction of the solar photon flux in the infrared. Indeed, Si PV modules

---

[1]Department of Chemical Engineering and Materials Science, Michigan State University, East Lansing, MI 48824, USA. [2]Ubiquitous Energy, Inc., Redwood City, CA 94063, USA. [3]Department of Physics and Astronomy, Michigan State University, East Lansing, MI 48824, USA. *e-mail: rlunt@msu.edu

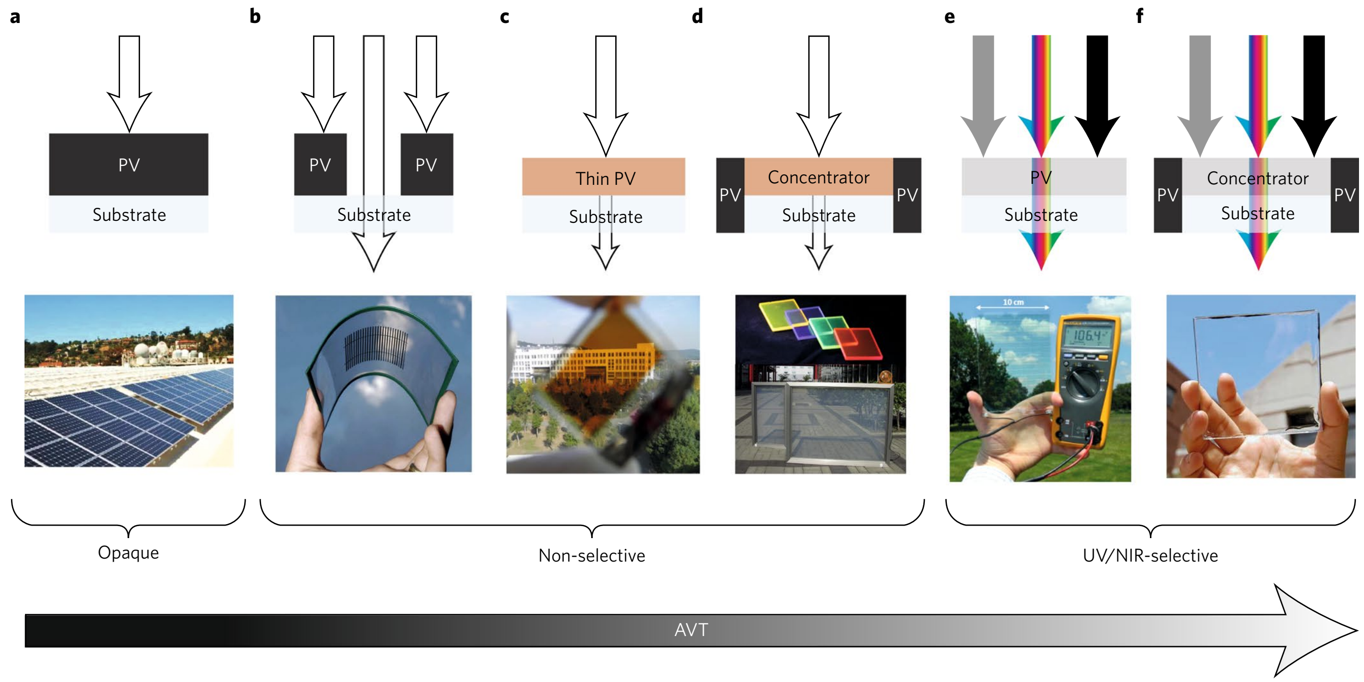

Fig. 1 | PV systems with various degrees of transmission. a, Diagram of a conventional opaque PV where full spectrum sunlight (represented by white arrows) is not transmitted and an example module. **b**, Diagram of spatially segmented PV and an example module. In a segmented architecture, opaque modules on a transparent substrate are spaced to permit partial transmission of all wavelengths of light. Increasing the space between modules improves transmission at the cost of performance as this essentially reduces the active area of the combined module. **c**, Diagram of a non-wavelength-selective, thin-film PV and an example perovskite-based module. In these architectures, the thickness of the optically absorbing film(s) is controlled to balance transmission and PCE, where increasing thickness improves PCE at the cost of partial transmission (narrow white arrows) and colour rendering. **d**, Diagram of a non-wavelength-selective solar concentrator, coloured LSCs and a scattering concentrator. LSCs and scattering concentrators collect light by absorbing, re-emitting, and waveguiding photons from a dye (LSCs), or by scattering incident photons (scattering concentrators) toward the edges of a substrate to be collected by edge-mounted PV strips. **e**, Diagram of a wavelength-selective TPV and a large-area, wavelength-selective TPV module. **f**, Diagram of a wavelength-selective LSC and a wavelength-selective LSC module. Wavelength-selective TPV technologies preferentially harvest UV (grey arrows) and NIR (black arrows) light while permitting the transmission of visible light (coloured arrows). Figures reproduced with permission from: **a**, Rick Naystatt, US Navy; **b**, ref. [100], Hindawi; **c**, ref. [101], American Chemical Society; **d**, ref. [102], Wiley (top), ref. [40], Elsevier (bottom).

generate more than half of their power from infrared photons. These thermodynamic efficiency limits are illustrated by the peaks of the 0% and 100% AVT curves in Fig. 2b, where each line represents the efficiency limit with respect to bandgap for a PV with a given fraction of absorption from the visible portion of the solar spectrum. Increasing the PCE above the single-junction SQ limit is feasible through the use of multi-junction architectures, where losses from electron thermalization are reduced or eliminated (Fig. 2c). The theoretical PCE limit for a realistic number of junctions (3–4) with 100% AVT is about 30% (ref. [10]). While this is comparable to the limit for single-junction opaque architectures, it is approximately half the limit for opaque multi-junctions. Even when practical limitations are considered (including resistive losses, charge recombination, diode non-idealities, parasitic electrode absorption; discussed in detail in refs [10] and [11]), it is estimated that single-junction and three-junction TPV solar cells fabricated with UV/NIR-selective materials can achieve 13% PCE and 20% PCE, respectively (assuming 10% loss in SQ photocurrent, 10% losses in the SQ fill factor and 20% loss in SQ photovoltage), approaching conventional PV technologies commercially available today, with almost none of the visible absorption.

Figure 3a shows a representative survey of published PCE values as a function of AVT (as calculated according to Box 1), for devices made using various wavelength-selective or non-wavelength-selective TPV device approaches (data presented in Fig. 3 may be found in Supplementary Data 1). The SQ limit in broadband-absorbing architectures varies sharply with AVT due to the inherent trade-off between performance and transmission, where PCE approaches zero as AVT approaches 100%. This is highlighted by the green and black lines, which show the SQ efficiency as a function of AVT for wavelength-selective and non-wavelength-selective PV, respectively. The shaded region between the two lines reflects the stark difference in maximum PCE achievable by using wavelength-selective over non-wavelength-selective TPV for AVT values greater than 50%. Additionally, all reported UV/NIR-selective TPV are from just the past 5–6 years, representing the rapid progress in terms of optimizing PCE and AVT simultaneously. As this field matures we expect more results to appear that approach, and eventually fall within, the shaded green region of the graph.

Current TPV technologies

TPV development has focused largely on segmenting opaque solar cells, reducing the thickness of otherwise opaque photoactive thin-films, or utilizing UV/NIR wavelength-selective photoactive materials to achieve visible transmission. In this section, we summarize the development of these approaches to TPV technologies.

Non-wavelength-selective, spatially segmented PV. Spatial segmentation is the practice of dispersing opaque solar cells across a transparent substrate. This approach provides varied levels of neutral optical transmission through the spaces between the solar cells (see Fig. 1b). Widening these spaces to increase transmission diminishes performance as this process reduces the photoactive area. While this method of achieving transparency has a low PCE limit at high AVT,

Box 1 | AVT and colour rendering

The recommended approach to reporting the AVT that is generally accepted by the window industry is to weight the integration of the transmission spectrum against the photopic response of the human eye[10,86], as:

$$\mathrm{AVT} = \frac{\int T(\lambda)P(\lambda)S(\lambda)\mathrm{d}(\lambda)}{\int P(\lambda)S(\lambda)\mathrm{d}(\lambda)}$$

where λ is the wavelength, T is the transmission, P is the photopic response, and S is the solar photon flux (AM1.5G) for window applications, or 1 for other applications.

For reference, the AVT for quartz glass is 92% and it has ~4% reflection from the front and back surfaces. A typical clear double-paned insulated glass unit[96] has AVT of near 80%. With a low emissivity coating, AVTs are typically ≤70%. The AVT in residential windows can range from 15% for highly tinted glass up to 90% for common clear glass. In general, glass with an AVT value above 60% looks clear, and any value below 50% begins to look dark, coloured, and/or reflective[97]. This gradual boundary also marks a transition in performance between demonstrated non-wavelength-selective and UV/ NIR-selective TPV architectures.

The figure of merit for transmitted colour is the colour rendering index (CRI), which describes quantitatively how accurately the colour of a given object is rendered either from a light source or through a transparent medium with respect to an 'ideal' illumination source (a blackbody radiator at a certain colour temperature, daylight illumination, AM1.5G, and so on) and is commonly used in the lighting and window industries. We note that for window applications the AM1.5G spectrum should be utilized as the reference spectrum. A comparison of a low and high CRI is shown in **a** (right). An illumination source or transparent medium with a CRI of at least 70 is considered to be of good quality and >85 to be of the highest quality[10,98]. For reference, a neutral or constant absorption profile through the visible spectrum will always yield a CRI of 100, regardless of the reference spectrum. CRI is of critical importance to glass, window, and display manufacturers.

Some applications also necessitate reporting the chromaticity coordinates directly, typically as a^* and b^* within the CIELab colour space (**b**, below) as is common in the window industry. Reporting a^* and b^* for transmission and reflection gives additional information regarding the perceived colour. High positive values of a^* and b^* are less common in modern window applications (yellow/red), whereas values near the origin (neutral/grey) and negative values of b^* (blue) are more typical if accompanied with high AVT. Quantitative examples of a^* and b^* are calculated for each of the transparent photovoltaic demonstrations in Fig. 5. The lightness (L^*) represents the human perception of contrast for given (a^*, b^*) coordinates, where a value of 0 is completely black and 100 is completely white. Additionally, the colour difference (ΔE^*) between normal and off-angle reflection should be minimized to prevent colour variations when viewing buildings from a distance with multiple viewing angles. Such colour variation is particularly evident if the chromaticity coordinates at different angles lie on opposite sides of the origin (that is, green to red for sign changes in a^* and blue to yellow for sign changes in b^*). Instructions for quantitative calculations of the CRI and chromaticity coordinates are given elsewhere[99].

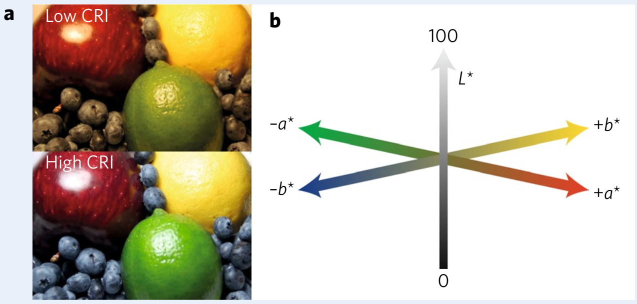

it can be used with essentially any opaque PV material. Research on spatially segmented technologies has been focused on silicon[12] and copper indium gallium selenide (commercialized by Sharp, Solaria, Sphelar, and Sunpartner Technologies) and more recently perovskite-based[13,14] materials (segmented on the microstructural level). Silicon-based architectures offer simple module fabrication as Si is commonly available and readily machined. Perovskite-based architectures are usually tolerant to defects and pinholes but have yet to show the high stability of Si[15].

Non-wavelength-selective thin-film PV. Non-wavelength-selective, thin-film PV use visibly absorbing semiconductors that are thin enough[16] or have a large enough bandgap[17,18] to permit the transmission of some visible light (see Fig. 1c), and are sometimes referred to as 'semitransparent'. Such thin-film devices are currently being commercialized (by Onyx Solar and Polysolar, for example). As is the case for spatial segmentation, broadband absorption always involves a direct trade-off between PCE and AVT. Si[19], CIGS[17], metal oxide[18], and perovskite-based[20,21] architectures have been the focus of most inorganic, non-wavelength-selective, thin-film TPV research. On average, these technologies feature PCE values between 0.1%[18] and 14%[21], AVT values up to 50%[18], and exhibit strong colour, which can be an advantage for some applications. There have also been a variety of demonstrations for single-junction organic PV (OPV) including small-molecule[22,23] or polymer-based[24,25] heterojunctions (commercialized by Heliatek), or dye-sensitized solar cells (commercialized by Dyesol)[26,27]. These devices have achieved at least 0.5% PCE[22] with AVT values between 25%[24] and 60%[26]. Non-wavelength-selective multi-junction architectures have exceeded 5% PCE, but typically exhibit AVT below 40% due to the high incremental visible absorption produced by the individual junctions[28,29]. The colour rendering indices (CRIs, discussed in Box 1) and demonstrated colours can be greatly varied because organic materials commonly absorb various parts of the visible solar spectrum[30].

Wavelength-selective thin-film PV. Visibly transparent technologies have recently emerged with excitonic materials that selectively absorb UV and/or NIR light (see Fig. 1e) and have often been referred to as 'transparent' and 'visibly transparent'. Such materials include organic small molecules, polymers, nanotubes, and salts. Optical absorption in organic and molecular semiconductors occurs in distinct molecular orbitals (S_1, S_2, … S_n) from the ground state (S_0) (Fig. 4a). The gap between the S_1 and S_2 levels can be exploited to allow visible light transmission and UV/NIR-selective absorption by controlling the molecular structure. By modifying the bandgap and the discontinuity of states it is possible to tune the solar harvesting outside of the visible band and into the NIR (Fig. 4b).

Efficient NIR-wavelength-selective TPV were demonstrated in 2011 with organic small-molecule planar heterojunctions consisting of chloroaluminum phthalocyanine (ClAlPc) as the donor

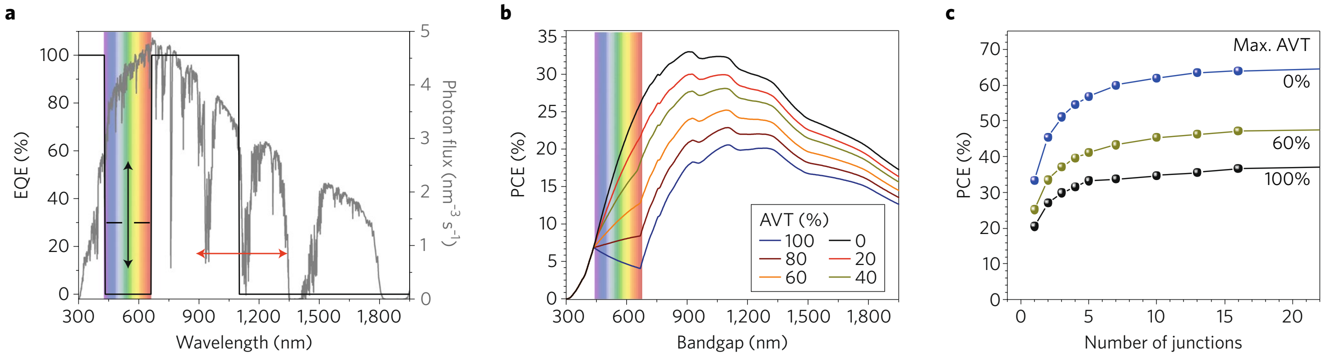

Fig. 2 | Theoretical performance limits for single- and multi-junction TPV. a, Schematic showing the ideal EQE for a wavelength-selective device, adjusted as a function of wavelength (red arrows) around the visible spectrum with varying degrees (black arrows) of visible EQE (dashed line). Note that in the thermodynamic limit the EQE is assumed to be equal to the absorption efficiency. The AM1.5 photon flux spectrum (grey) indicates the large amount of NIR light available for wavelength-selective harvesting. **b**, PCE plotted as a function of the absorber bandgap for various levels of visible light contribution to the EQE in a single junction. **c**, Theoretical PCE limits at 1-sun intensity plotted as a function of the number of junctions in a multi-junction architecture at 0%, 60%, and 100% AVT. PCE values are calculated in ref. [10]. A maximum of 3–4 junctions is typically explored for current record efficiency multi-junction devices. Data for **b**,**c** from ref. [10].

and C_{60} as the acceptor (Fig. 5a–c) sandwiched between two transparent conductive electrodes (indium tin oxide, ITO)[31]. Through optimization of the optical interference from the top ITO thickness, a PCE of 1.3±0.1% and AVT of 65% were achieved, the highest combination achieved at the time. A PCE of 1.7±0.1% and AVT of 56% were obtained with the use of NIR-reflecting mirrors. High-efficiency polymer-based wavelength-selective TPV were demonstrated in 2012 utilizing bulk heterojunction (BHJ) architectures of poly(2,60-4,8-bis(5-ethylhexylthienyl)benzo-[1,2-b;3,4-b] dithiophene-alt-5-dibutyloctyl-3,6-bis(5-bromothiophen-2-yl) pyrrolo[3,4-c]pyrrole-1,4-dione) (PBDTT-DPP) and phenyl-C_{61}-butyric acid methyl ester (PCBM)[32]. The top electrode consisted of a combination of Ag nanowires and ITO nanoparticles that resulted in a PCE of 4% and an AVT of 64% (Fig. 5d–f). Figure 5g–i shows the highest third-party-certified (Newport) wavelength-selective TPV PCE we are aware of to date (Ubiquitous Energy). This single-junction device utilizes an NIR-selective excitonic semiconductor with a broad photoresponse between 650 nm and 900 nm. The PCE reaches 5.1% at greater than 50% AVT, with an open circuit voltage (V_{oc}) of 0.7 V, approaching the theoretical limit for the bandgap. This wavelength-selective TPV device architecture has also been scaled via vapour deposition into functional large-area modules up to one square foot, comprising monolithic series-integrated subcells (see Figs. 1e and 5g). Wavelength-selective TPV fabricated with polymer donors and small-molecule acceptors were recently demonstrated with PCE values of 7.7% (ref. [33]) and 9.8% (ref. [34]), albeit with AVTs of only 26% and 32%, respectively (calculated according to Box 1). Most of the broad optical absorption exhibited by these architectures encompasses NIR wavelengths, as indicated by their high NIR external quantum efficiency (EQE). These demonstrations therefore establish important molecular approaches for TPV with lower bandgap photoactive materials, broad optical absorption, and high EQE.

These studies are important in not only demonstrating the feasibility of this wavelength-selective approach to TPV, but also in highlighting the importance of photon management. Managing reflections throughout the spectrum becomes particularly important in TPV, as reducing visible reflections and absorption are both equally key to maximizing transmission. Minimizing visible reflection requires optimization of the optical interference across the layers of the TPV. In contrast, for NIR wavelengths reducing NIR reflections at the front-side contact and increasing backside NIR

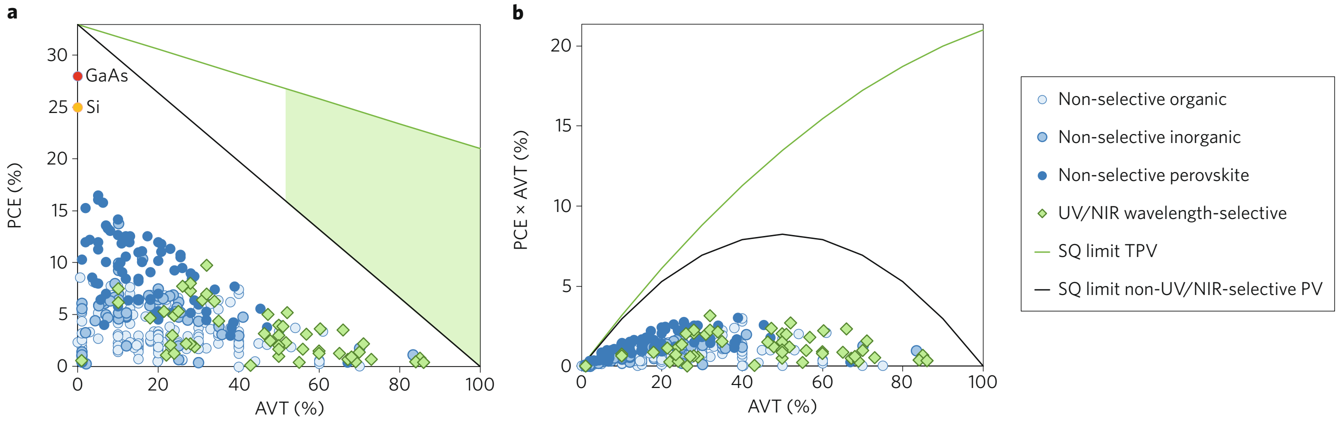

Fig. 3 | Survey of TPV. a, PCE versus AVT for wavelength-selective and non-wavelength-selective organic, inorganic, and perovskite TPV technologies. Wavelength-selective TPV have peak absorption in the UV and NIR portions of the spectrum. **b**, Plot of the light utilization efficiency (LUE, defined as the product of PCE and AVT, see Equation 4) versus AVT. References for the complete survey are provided in Supplementary Data 1. The green shaded region in **a** denotes the target PCE and AVT only achievable with UV and NIR TPV solar technologies. The red and yellow points in **a** represent the record PCE for GaAs and Si-based single junction PV respectively.

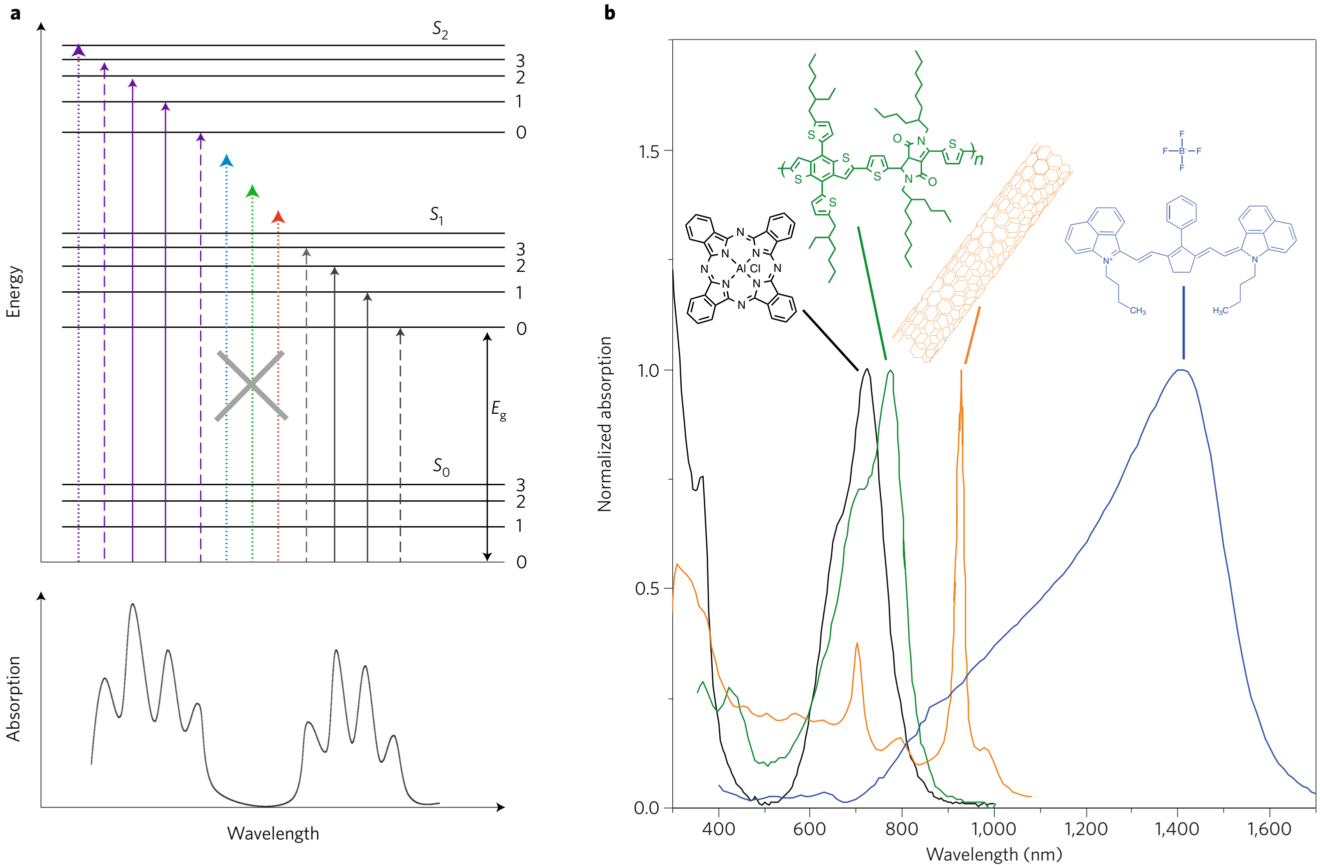

Fig. 4 | Selective optical absorption. a, An energy schematic for an excitonic material depicting the ground state (S_0) and the two lowest occupied molecular orbitals (S_1, S_2). The overlap of vibrational modes determines the intensity of absorption, which may be weak (dotted arrows), moderate (dashed arrows), or strong (solid arrows). The gap between excited molecular orbitals creates a discontinuity in the density of states, yielding a band of transmitted light between absorption peaks. Coloured portions of the absorption spectrum shown here correspond to the coloured arrows representing absorption. The energy gap (E_g) is defined between the lowest vibronic states of S_0 and S_1. **b**, Absorption profile of NIR-selective harvesting molecule films including: (1) small-molecule, ClAlPc (black); (2) polymer, PBDTT-DPP (green); (3) nanotube, a (9,1) carbon nanotube (orange); and (4) organic salt cation (1-Butyl-2-(2-3-2-(1-butyl-1H-benzo[cd]indol-2-ylidene)-ethylidene-2-phenylcyclopent-1-enyl-vinyl)-benzo[cd]indolium) paired with BF_4 (anion) (blue). The molecules were demonstrated in refs [31] (1), [32] (2), [103] (3), and [80] (4).

reflections can be utilized to enhance NIR photoconversion without impacting the AVT.

Current concentrator technologies

Solar concentrators utilize dyes or scattering effects to capture incident light normal to a substrate surface and redirect it toward the edges to be harvested by conventional PV. In this section, we discuss the development of luminescent solar and scattering concentrators.

Non-wavelength-selective and colourful LSCs. LSCs offer another promising approach to lowering the cost of PV systems and have been used in colourful (non-wavelength-selective) devices, and more recently, in plain window glass (wavelength-selective). An LSC consists of a substrate coated or embedded with an organic dye (or luminophore) that redirects incident light to the edges through photoluminescence[35] (see Fig. 1d). Thin strips of conventional PV mounted along the waveguide absorb the waveguided light and generate power with a PCE limit equivalent to non-wavelength-selective TPV when there is ideal light trapping[36]. As with other PV technologies, the PCE for LSCs and other concentrators is defined as the ratio of electrical power to the incident solar power on the module area, although many studies only report the optical efficiency. These can be distinguished by the equation $\mathrm{PCE} = \eta_{\mathrm{Opt}}\eta^{\star}_{\mathrm{PV}}$, where η_{Opt} is the optical efficiency (the ratio of the photons transported out of the LSC edge to the incident photons on the active area) and $\eta^{\star}_{\mathrm{PV}}$ is the PCE of the edge-mounted solar cell under monochromatic illumination from the luminescent emitter. Care should be taken to distinguish reports of the optical efficiency and the PCE as they are often different by an order of magnitude[36]. The optical efficiency is defined as $\eta_{Opt} = (1 - R_f)\eta_{Abs}\eta_{PL}\eta_{Trap}\eta_{RA}$ where R_f is the front-face reflection, η_{Abs} is the absorption efficiency, η_{PL} is the luminescent efficiency, η_{Trap} is the waveguiding efficiency, and η_{RA} is the efficiency of suppressing reabsorption. Most organic-based LSCs exhibit colourful optical transmission due to the discrete visible absorption, but PCE values up to 7% have been reported over small LSC surface areas[37]. Newer quantum dot (QD)-based LSCs exhibit broader visible absorption and retain colourful transmission, but are often limited by the same performance-transmission trade-off as other inorganic thin-film technologies[38,39].

Non-wavelength-selective scattering concentrators. Scattering concentrators consist of light-scattering media deposited into or onto clear waveguiding substrates. Optical wavelengths shorter than the feature size are scattered, yielding a visibly hazy surface (see Fig. 1d), with some of the scattered light waveguided to the edges of the substrate, where it is harvested by thin PV cells[40]. However, the main challenge for scattering concentrators is that optical losses are significant at area scales above a few inches due to the multiple

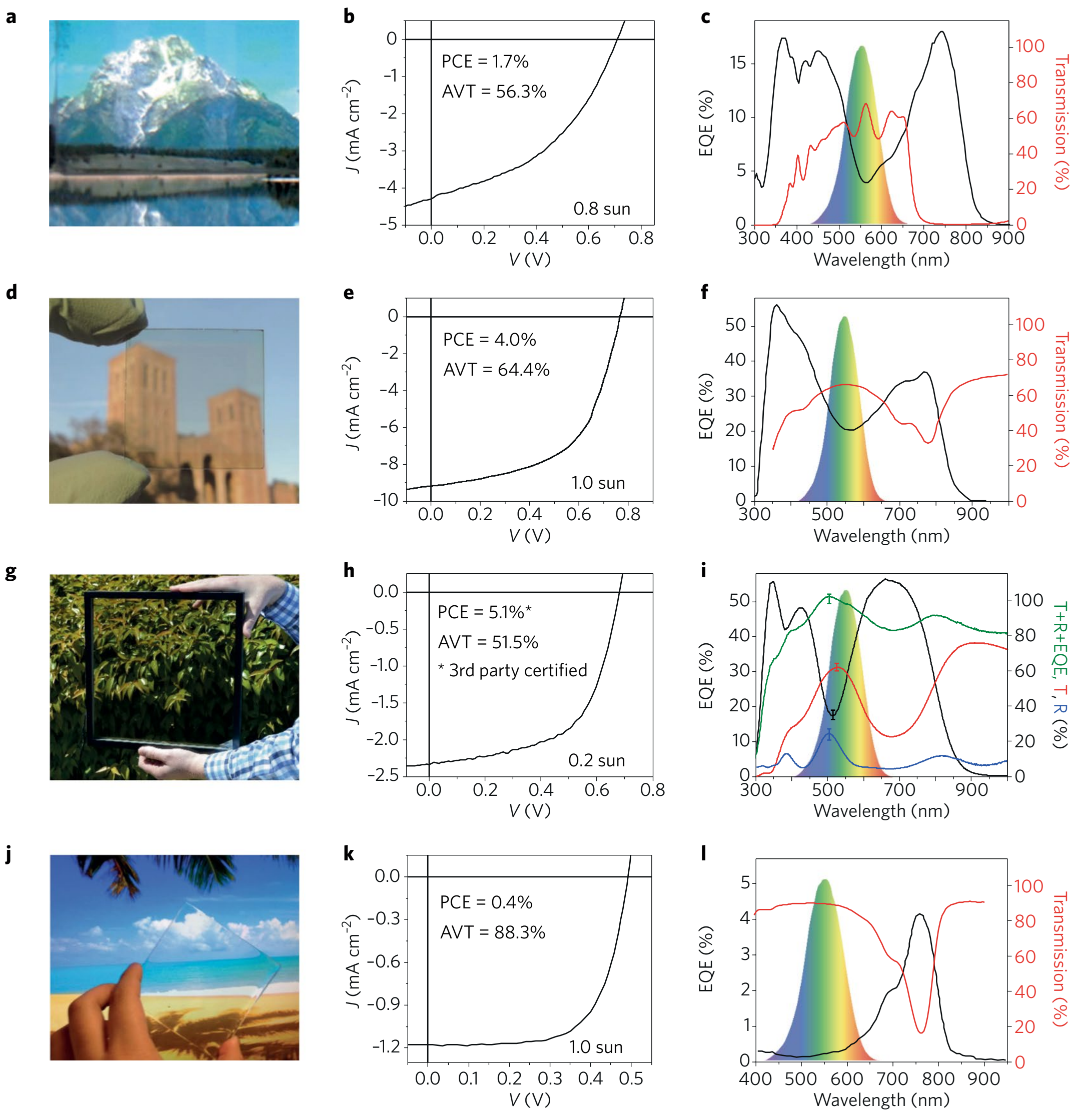

Fig. 5 | Wavelength-selective TPV and LSC with >50% AVT. a–c, Photograph of the first wavelength-selective TPV device based on small molecules (12-cells, series-integrated mini-module) (**a**), the single cell current (J) voltage (V) characteristics (**b**) and the EQE and optical transmission characteristics (**c**). **d–f**, A high-efficiency single-junction polymer-based wavelength-selective TPV (**d**) with corresponding J–V (**e**) and EQE and transmission (**f**) characteristics. **g**, Photograph of series-integrated wavelength-selective TPV module. **h**,**i**, A Newport-certified record efficiency single-junction wavelength-selective TPV cell (Ubiquitous Energy); **h**) with the corresponding T, R, EQE, and photon balance ($T + R +$ EQE) for the TPV cell (**i**). The error bars represent the uncertainty in measurement of R (4%), EQE (2%), and T (2%) across the full spectrum of each measurement (propagated uncertainty on the sum is ~5%). **j–l**, An efficient, wavelength-selective NIR-absorbing transparent LSC (TLSC; **j**) with J–V (**k**), EQE, and transmission (**l**) characteristics. Also shown in the middle panels are the PCE and AVT (calculated according to Box 1) for each demonstration. The photopic response is also shown in panels **c**, **f**, **i**, and **l** as a rainbow-coloured area to show the visible spectrum. CRI and transmitted colour coordinates (a_{T}^*, b_{T}^*) were calculated from the transmission spectra as follows. CRI: 95.7, a_{T}^*: –3.4; b_{T}^*: 10.4 (**c**); CRI: 94.5, a_{T}^*: –5.0 ; b_{T}^*: 7.0 (**f**); CRI: 65.3, a_{T}^*: –27.7; b_{T}^*: 8.2 (**i**); CRI: 94.3, a_{T}^*: –3.9; b_{T}^*: –0.22 (**l**). Positive and negative values of a_{T}^* represent green and red, respectively, while positive and negative values of b_{T}^* represent yellow and blue respectively in the CIELab colour space (Box 1). Figures reproduced with permission from: **a**, ref. [31], AIP publishing; **c**, ref. [31], AIP publishing; **d**, ref. [32], American Chemical Society; **j**, ref. [42], Wiley. Data for **b–c** from ref. [31], for **e–f** from ref. [32], and for **k–l** from ref. [42].

scattering events of the waveguided photons, which can result in sizeable losses via outcoupling from the device. While the intrinsic visible haziness limits adoption in many applications requiring an unobstructed view, these could become important in areas for higher privacy.

Wavelength-selective transparent LSCs. Recently, a parallel approach to fabricate wavelength-selective TPV was demonstrated[41,42] using an LSC with wavelength-selective luminophores that could both absorb and emit outside of the visible band. This approach could simplify the manufacturing and scale-up processes for wavelength-selective TPV while also providing a route to very high transparency levels and low module costs. Wavelength-selective LSCs may be designed to absorb UV and emit NIR light or absorb NIR and emit deeper NIR light. Although NIR-absorbing LSCs achieve similarly high AVT and CRI values to UV-absorbing LSCs, reabsorption becomes a challenge when scaling to sizes at or above square metres, as is the case for traditional LSCs.

The first wavelength-selective LSCs were fabricated with phosphorescent luminophores consisting of hexanuclear metal halide nanoclusters with selective harvesting in the UV and emission in the NIR. Using these materials, PCE values >0.5% were achieved yielding a high AVT (>85%) and CRI (>95) approaching that of bare glass[41]. As a by-product of the large spectral shift (~400nm), reabsorption losses in these LSCs were essentially eliminated. However, owing to the lower fraction of UV photons in the AM1.5 spectrum, the maximum PCE of these devices is less than 7% (ref. 36). Other demonstrations of UV-selective organic[43] and quantum dot[44] luminophores have also been demonstrated, albeit with visible light emission that creates a colourful glow. More recently, organic salt derivatives were demonstrated in NIR-selective absorbing and emitting LSCs that achieved PCE values >0.4% (Fig. 5j–l), high AVT of 88%, and CRI >94 (ref. 42). Following a similar approach, Si naphthalocyanine (SiNc) was utilized to fabricate LSCs that selectively harvest both UV and NIR light to achieve an η_{Opt} of 1.5% (ref. 45). As discussed below, most LSCs (including wavelength-selective LSCs) are limited predominately by reabsorption losses that need to be reduced before these technologies are scaled to the largest module sizes.

Key challenges for wavelength-selective TPV and LSCs

Wavelength-selective TPV and LSCs face the same development challenges as their non-wavelength-selective counterparts. In this section, we discuss strategies for overcoming excitonic limitations, optical losses, resistive losses, and air sensitivity to approach high PCE values.

TPV exciton diffusion bottleneck. Reviews on excitonic and OPV can be found elsewhere[46,47]. We briefly summarize here the key points relevant for TPV research. Most excitonic materials exhibit modest exciton diffusion lengths (EDLs; approximately 10–20 nm) for both singlet and triplet excitons[48,49]. In PV configurations, this limits the thickness of the active layer to balance optical absorption efficiency and internal quantum efficiency (IQE, electrons collected per absorbed photon) in planar heterojunctions. BHJs are an important approach to circumvent the exciton bottleneck by introducing an interpenetrating network of donor and acceptor molecules with feature widths comparable to the EDL[50]. However, longer-term solutions could be achieved with the enhancement of the EDL, as recently demonstrated through molecular templating[51], altering molecular packing arrangements[52,53], and tailoring crystalline order[54].

Transparent electrodes. Scaling TPV to the sizes necessary for window integration with minimal reductions in performance requires improvements in transparent electrode conductivity, element abundance, defect tolerance, and patterning. Transparent conductive oxides (TCOs) such as ITO exhibit higher resistivity compared to metallic electrodes. While adding metallic grids can improve conductivity (often at the cost of transmission)[55], upscaling devices to the largest sizes without substantial PCE losses remains a challenge. The sputtering processes required to deposit many metal oxides also potentially introduces shunting pathways that could reduce device yields.

Polycrystalline ITO often yields brittle films that can be problematic for flexible devices such as laminated window coatings, discussed below. Ideally, future oxide-based transparent electrodes will consist of amorphous, low-resistivity materials that can be easily deposited. Amorphous ITO derivatives including InZnAlO (ref. 56), InZnO (ref. 57), InZnSnO (ref. 58), $ZnSnO_3$ (ref. 59) and InSiO (ref. 60) retain moderate conductivity and have been demonstrated recently as potential electrodes in flexible devices. Regarding abundance, In is sometimes considered an element that is in high demand, with potentially limited sources in the future. However, the popularity of other In-containing technologies for optoelectronics applications such as CIGS, LCDs, and touchscreens indicates the viability of its use, where increased recycling of In can help to mitigate any future availability concerns[61,62]. Nonetheless, there is considerable ongoing work to develop In-free electrodes and TPV need not be constrained to only In-based electrodes. Thin metallic films, nanowires, and nanotubes are promising alternatives that offer good ductility and conductivity[63]. However, many architectures are subject to damage from the solution-based processes required to integrate nanowires and nanotubes. Thin metallic films can be thermally deposited but conductivity and transmission need to be balanced because discontinuous films formed at low thicknesses yield high resistivity.

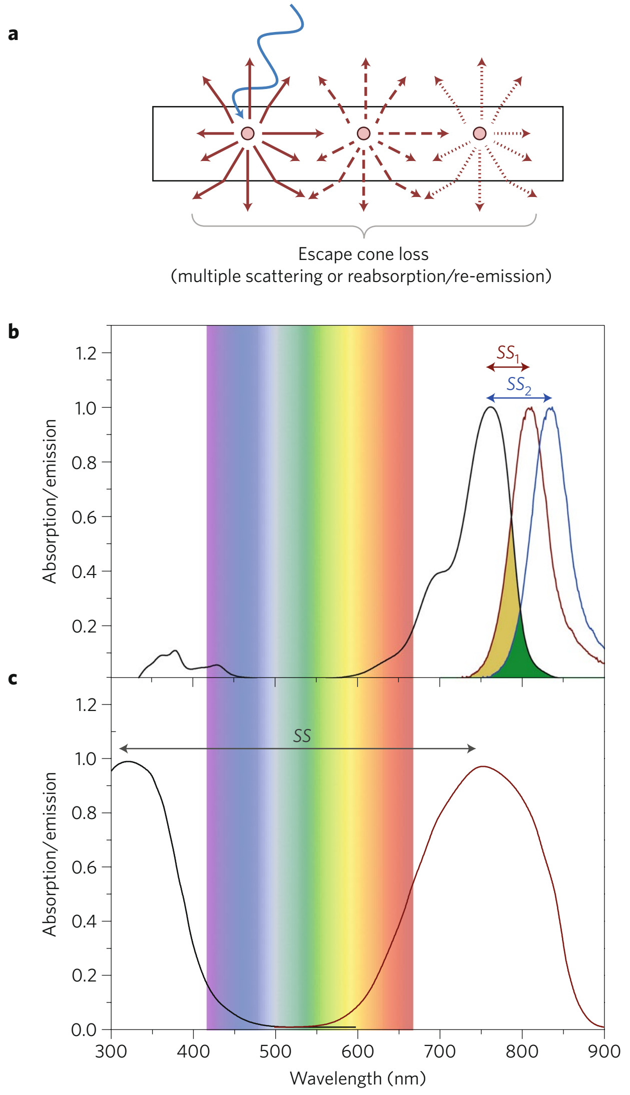

Fig. 6 | Loss mechanisms for luminescent and scattering solar concentrators. a, Schematic illustrating multiple scattering or reabsorption/re-emission losses in an LSC. Following initial excitation (blue arrow), photons can be lost through scattering or re-emission through the escape cone (solid red arrows). These losses are compounded by each subsequent re-absorption/re-emission or scattering event even with a luminescence efficiency of 100% (dashed and dotted red arrows). **b**, Absorption (black) and emission (red and blue) spectra for an NIR-absorbing/NIR-emitting wavelength-selective TLSC with the respective Stokes shifts (SS_1 and SS_2) highlighted. Reabsorption losses are more likely to occur at small SS values (SS_1) than larger values (SS_2) due to greater overlap (shaded yellow region) between absorption and emission for SS_1 than SS_2 (shaded green region).**c**, Absorption (black) and emission (red) spectrum for a UV-absorbing/NIR-emitting TLSC based on down-converting nanoclusters with the Stokes shift highlighted. Data for **b** and **c** from ref. 36.

Stokes shift efficiency for wavelength-selective LSCs. Reabsorption losses, that is, the loss of emitted photons that are reabsorbed by luminescent dyes as shown in Fig. 6a, are typically the dominant loss mechanisms in LSC technologies and are impacted directly by the Stokes shift (the difference between the absorption and emission peaks of the luminophore, shown in Fig. 6b), η_{Trap}, η_{PL} and the device length. In the NIR-absorbing LSCs demonstrated in ref. [42], the EQE (electrons generated per incident photon) of the full device, including the edge-mounted solar cell, decreases rapidly as plate size is increased due to reabsorption losses from a small Stokes shift. This highlights the key importance of the Stokes shift in scaling any LSC to large size, which is as crucial as the luminescent quantum yield. If the Stokes shift is increased to >100 nm (Fig. 6c), LSC sizes could be increased to over 1 m^2, enabling adoptability in nearly all envisioned applications[64]. The key materials design challenges to achieving this goal have recently been summarized[36].

Angle dependence. Losses from oblique illumination must also be considered for building integration as few surfaces (including roofs) remain at ideal incidence for long periods of the day. Nonetheless, there has already been considerable interest in the solar research community in creating three-dimensional structures such as solar towers to enhance solar collection[65]. These structures can collect substantially more total sunlight than solar tracking units of an equivalent rooftop footprint. For example, the total solar flux density from all four sides of a vertical building in Boston (9.3 kWh per vertical m^2 per day) is substantially more than for a solar tracking unit of equivalent footprint (6.0kWh per horizontal m^2 per day)[66,67], and even greater if we account for the total vertical area utilized in the building; while south-facing vertical windows will give the highest solar flux and therefore highest power output and lowest levelized cost of electricity (LCOE) per installed area, east–west facing windows extend the useful power production throughout the day. Data on the orientation-dependent solar flux for various locations is provided in Supplementary Data 1.

Parasitic reflections at oblique angles can be reduced or nearly eliminated by controlling various layer thicknesses[68–70]. For example, a wavelength-selective TPV with optimized active layer and top ITO thicknesses can retain 80% of its normal-incidence performance[68] under an illumination angle of up to 80°. This translates into an increased annual power output for a south-facing window of 15–40%, depending on location[69]. While optional NIR mirrors can also be sensitive to angle variations, more advanced designs have been demonstrated commercially that reduce or eliminate oblique angle variations in reflection[71]. In the case of LSCs, the nature of light absorption intrinsically reduces the impact of angle dependence to a single front-side reflection, allowing for harvesting of both direct and diffuse light with little angle dependence[35].

Lifetime. An important challenge for any emerging PV technology, and particularly for nanostructured materials, is device lifetime. Organics and QD nanocrystals, for example, can react with oxygen and/or moisture. Because TPV enable deployment in new applications, a more important question arises, that of the precise lifetime requirements. In the case of many mobile electronic devices, practical device lifetimes are less than 10 years. For buildings and windows, we recognize that no PV technology lasts as long as a building and this becomes a question of replaceability. TPV applied in windows could be installed and replaced as laminates on the inside of windows — similar to the way overhead lighting is typically replaced every 2–3 years. The specific lifetime targets and replacement logistics for TPV laminates will ultimately be defined by both the energy and cost payback times. Considering that energy payback for many organic PV technologies can be as low as months or weeks[72], organic technologies with the range of projected lifetimes already demonstrated (1–25 years or more)[73,74] have great potential for use in TPV both for added functionality and as a renewable energy source. Although nanostructured materials are reputed to be more sensitive, commercialized organic light emitting diodes (OLEDs) and quantum dot light emitting diodes (QD-LEDs) are beginning to change that perception thanks to efficient encapsulation strategies. Red fluorescent OLEDs have recently reported lifetimes in excess of 1 million hours at 1,000 cd m^{-2}. Indeed, extrapolated lifetimes for OPV of >25 years (the accepted benchmark for traditional PV) in an oxygen-free environment have already been reported. It is noted, however, that long lifetimes are unusual for current technology; many demonstrations fall well short of this metric with extrapolated lifetimes of 2 years[75] and typical non-extrapolated lifetimes of 1.5 years or less[76,77].

While lifetimes specific to wavelength-selective TPV have yet to be reported, these demonstrations provide an indication that organic molecules are viable for long-term applications. At present, all PV module technologies are encapsulated. Despite cavity glass encapsulation being less suitable for flexible applications, thin-film barrier layers and flexible glass could lead to comparable protection from oxygen and moisture without compromising flexibility or transmission[78].

Multi-junctions. Multi-junctions are a route to reaching the highest PCE for traditional PV and are similarly important for TPV. These architectures consist of current-matched complementary UV- and NIR-absorbing subcells connected in series. Although this approach to enhance efficiencies has been demonstrated with many opaque and non-wavelength-selective devices[79], it has yet to be fully explored with wavelength-selective TPV and LSCs at the highest AVT values. Multi-junctions can be optimized for oblique illumination in the same manner as single junctions, however this can be challenging if the individual subcells exhibit separate angle dependencies. In these cases, the current-limiting subcell mounted on a vertical facade would probably change over the course of a day, yielding potential reductions in device performance.

The development of multi-junction cells also requires a greater catalogue of bandgaps with selective absorption deep into the NIR. This is a considerable challenge due to energy level alignment and typical exciton binding energies of 100–300 meV (ref. [80]). As donor and acceptor bandgaps are further reduced for deeper NIR absorption, low interfacial gaps (the energetic offset between the highest occupied molecular orbit (HOMO) of the donor and the lowest unoccupied molecular orbit (LUMO) of the acceptor) could make it difficult to balance the energy offset needed to dissociate excitons while also maintaining a high V_{oc}. One approach to solve this problem utilizes organic salts[81], in which the frontier orbitals can be sensitively tuned via anion blending to maximize both photocurrent and photovoltage without changing the optical absorption of the cation[82]. At small enough bandgaps these binding energies could exceed the driving force for exciton dissociation unless the interfacial gap (and thus V_{oc}) is reduced. Strategies to minimize the binding energy include delocalization of the HOMOs and LUMOs through molecular asymmetry to increase the exciton radius (inversely proportional to binding energy)[83] or condensing HOMOs and LUMOs to raise the dielectric constant[84]. Nonetheless, photoresponse with such organic salt molecules has been demonstrated with response as deep as 1,600 nm (refs [80,85]).

How to measure and report TPV performance

TPV necessitate unique standardized approaches to characterization and reporting. While the PCE values for TPV are defined in exactly the same way as any other PV technology, PCE measurement warrants additional consideration as TPV are intrinsically bifacial and allow illumination from both sides. The PCE measurement for TPV should therefore be standardized with a matte black background behind the cell to eliminate backside illumination from the test environment or reflection (double pass) from a solar simulator.

Regarding transparency measurements, many articles on TPV report average visible transparency based on averaging the transmission spectra over an arbitrary wavelength range and transmission spectra measured with reference samples that are not needed for the absolute transmission measurement of the entire device. The AVT should instead be reported as the integration of the transmission spectrum weighted against the photopic response of the human eye as accepted by the window industry[10,86] and discussed in Box 1. The CRI is equally as important to glass, window, and display manufacturers not only because of aesthetics, but due to its potential effect on the human circadian rhythm[87]. Photosensitive ganglion cells in the eyes of mammals, linked directly to the control of the circadian rhythm, are highly sensitive to the blue region of the visible spectrum. This sensitivity and its potential physiological effects on building inhabitants can leave PV technologies with low AVT or CRI unfit for many widespread window applications.

The last key consideration in characterizing and reporting TPV is the photon balance at every wavelength:

$$A + R + T = 1 \tag{1}$$

where A is the absorption, R is the reflection, and T is the transmission of the TPV. For spatially segmented PV this includes both absorbing and transmitting areas. Owing to difficulties in measuring A directly, this can be obtained from:

$$A = \frac{\mathrm{EQE}}{\mathrm{IQE}} + A_{\mathrm{Contact}} \tag{2}$$

where A_{Contact} is the parasitic absorption in the contact layers (close to 0 for LSCs), and the EQE can be measured directly. In the limit of IQE = 1 (a reasonable approximation for some BHJ and ultra-thin planar architectures) the minimum absorption spectrum can then be estimated from the EQE. In this approximation, the following equation should be satisfied at every wavelength with independent measurements of EQE, R, and T:

$$\mathrm{EQE} + R + T \leq 1 \tag{3}$$

Alternatively, an estimate of the IQE can be obtained from a similarly designed opaque device where A is estimated from R measurements and applied to equations (2) and (3) or obtained from optical interference simulation fitting of EQE on opaque devices[88]. Another approach to estimate absorption is to measure the EQE under reverse bias to extract the absorption in the active layer[89]. We note that the balance is still valid for multi-junction cells, where EQE is typically reduced to produce a greater voltage; in this case, the IQE of the total device is reduced (requiring multiple photons to obtain one electron at a higher potential). The minimum absorption could then be estimated by summing the reverse-biased EQE of each subcell under optical biasing of the other subcells. While in opaque cells this balance is much simpler and requires only measuring R (to obtain $A = 1 - R$), the addition of the transmission term has created confusion in many reports that have not been shown to satisfy this balance. An example of this simple consistency check is shown for the wavelength-selective TPV device in Fig. 5i. Thus, we encourage all reports on TPV to provide independent EQE, R and T measurements for each device to allow such validation and alleviate concerns over experimental errors. This consistency check should become standard for all PV with any visible light transmission, similar to the now-standard check of integrating the EQE to confirm the measured short circuit current density (J_{sc}) for any PV technology.

A new figure of merit for TPV

Although PCE and AVT are often inversely related as discussed above, all TPV technologies have potential applications. Progressive development warrants new compound figures of merit beyond PCE and AVT that allow for improvements to be referenced across various technologies. We propose a light utilization efficiency (LUE) metric:

$$\mathrm{LUE} = \mathrm{PCE} \times \mathrm{AVT} \tag{4}$$

This metric enables comparison between technologies against theoretical limits and also represents an overall system efficiency: for example, in a window or display application this would be the combination of generated power efficiency and overall lighting efficiency (that is, the transmitted light per incident lighting power). A device with a high LUE could be applied over a window to provide power without blocking natural light from entering the room to reduce the need for artificial lighting during daylight hours[90]. Similarly, such a device applied over an electronic display would offset energy consumption without requiring additional brightness from the display to compensate for absorbed visible light. This quantitative applicability comparison would provide greater insight into the importance of future demonstrations than PCE or AVT alone. We note that for particular applications there are often also key individual thresholds for AVT, PCE, and CRI that also motivate development of application-specific figures of merit that provide weighting or limits on all three metrics. For this reason, new figures of merit could be important moving forwards, but should supplement and not replace independent reporting of each component metric. Ultimately the LUE adds to the list of important PV metrics that have emerged including, for example, the LCOE (measured in US\$ per kWh) and specific power (in W g^{-1}).

The survey and theoretical limits from Fig. 3a are plotted as the LUE versus AVT in Fig. 3b. Based on the theoretical limits for wavelength-selective TPV discussed above (and in ref. [10]), the maximum LUE for single and multi-junction cells (100% AVT) are 20.6%, and 37%, respectively. This plot shows the total system potential for each approach to creating transparency in PV devices and highlights that the maximum LUE can be achieved by wavelength-selective harvesting. In the future, the LUE will serve as an important guide to map the progress of high-efficiency TPV that is comparable across the full range of enabling technologies and is utilized to help define entry-level performance discussed in the Outlook section.

Outlook

The emergence of highly transparent PV represents a new paradigm in PV deployment, opening solar markets to approach the installed area necessary to substantially offset fossil-fuel consumption worldwide. Achieving widespread adoption requires the compound optimization of PCE, AVT, and CRI. Ultimately, wavelength-selective and non-wavelength-selective TPV technologies are unlikely to be direct competitors, but will probably find complementary applications and markets on the basis of their unique performance space (see Fig. 7b).

While electronic displays require AVT >80% (LUE >5%), tinted architectural glass requirements typically start closer to 50%. PCE values of 5–10% (LUE >2.5%) will be required to achieve a competitive LCOE (see Supplementary Data 1) in BIPV applications, however, 2–5% PCE (LUE >1.5%) is sufficient to self-power low-power mobile electronic devices. TPV with a similar PCE but lower AVT (LUE >1%) can self-power smart windows or complement passive window coatings (with low-emissivity) or smart window technologies (electrochromic windows). TPV have already demonstrated the ability to achieve beyond these entry application thresholds.

Building windows coated with TPV enable electricity generation to offset building's electricity consumption, to autonomously power electronic smart window technologies, and reduce incident heat load. TPV can be designed to selectively absorb UV[41,91] or deep NIR[80] light to work in concert with visible- or NIR-selective smart

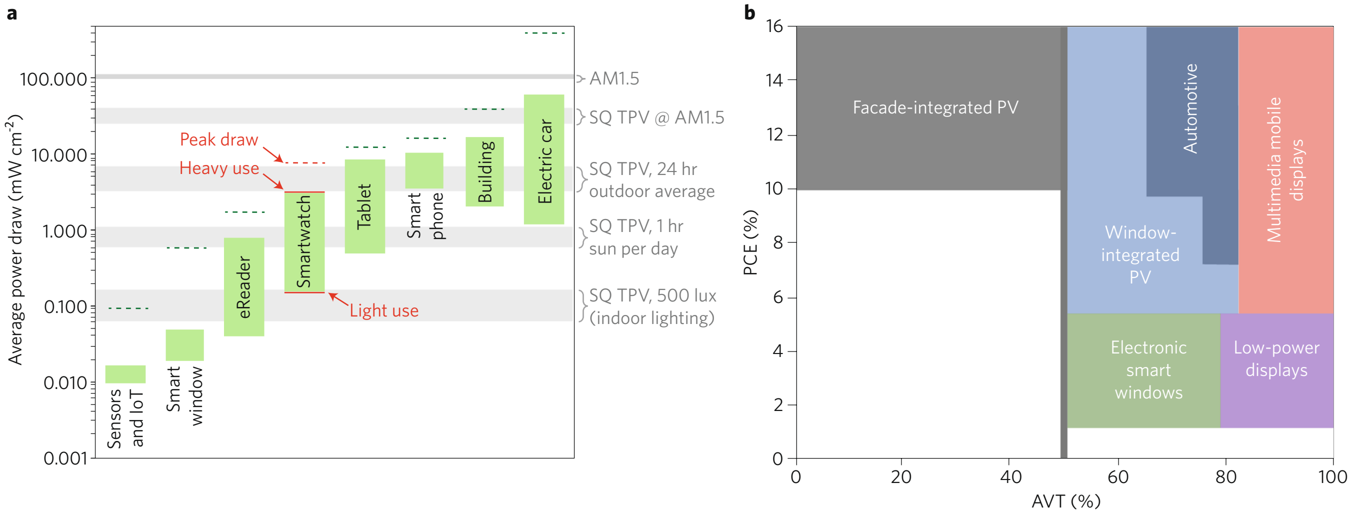

Fig. 7 | Integration requirements. a, Average power draw per device surface area applicable to TPV for various applications ranging in power draw from the Internet of Things (IoT) to electric cars. The shaded green bars correspond to the devices' average power draw (total energy consumption averaged over the full use profile, including representative periods of use and non-use), with the range capturing differences between user types and brands. An average TPV power output that is higher than the average power draw results in a completely autonomous device (infinite battery life), whereas a lower power output results in battery life extension. For comparison, the shaded grey bars show the power output of an SQ TPV under various illumination conditions. Dashed lines are also included for reference to show a representative peak power draw for each device type during full use (for example, when the display is on). **b**, Application requirements for TPV as a function of PCE and AVT. Tinted architectural glass is typically at least 50% transparent, whereas electronic displays require an AVT of at least 80%. PCE values of 2–5% are sufficient to autonomously power smart windows and low-power displays, whereas PCE values of at least 5–10% are required to power mobile displays or achieve competitive LCOE to match semitransparent modules in automotive and building-integrated applications.

window technologies[92,93]. A window enhanced with a TPV coating can also replace or be combined with low-emissivity coatings, which reflect NIR light. In terms of the overall electricity potential, we estimate that there is approximately 5–7 billion m^2 of glass surface in the United States. Equipping this area with 15% PCE TPV (with an average flux of approximately 2.7 kWh m^{-2} per day across all faces in vertical configurations and skylights in a horizontal configuration) this would approximately output an additional 100 GW, which approaches the rooftop potential and could be substantially augmented if also integrated in the non-glass siding of buildings.

TPV have also caught the attention of the automotive industry[94,95]. Well in advance of the 10–15% PCE values (LUE >6.5%) that a TPV-coated electric vehicle would need to extend its range by 10–20 miles a day with only solar energy, auto makers are now looking at incorporating TPV on a smaller scale. A TPV-coated sunroof, for example, could power fans or maintain the tinted state of an electronic tinting (that is, in a smart window) to cool a car parked in the sun.

Integrating TPV across the surface of electronic displays can enable extended use by charging the batteries of the device while maintaining a view of the display. In low-power wearables and e-readers, TPV could eliminate the need to ever connect to a charger. The impact of TPV on battery life is assessed by comparing the average power draw of the electronic device to the average power output produced by the PV across use conditions, as illustrated in Fig. 7a.

The estimated performance requirements for TPV are mapped in Fig. 7b across various applications. Wide-scale deployment will require further improvements in long-term durability and electrode conductivity. However, the path towards large-area commercialized wavelength-selective TPV is achievable given that many glass manufacturers already employ in-line deposition systems for a range of multilayer glass coatings. With preliminary TPV demonstrations already exceeding the PCE, AVT, and LUE metrics for architectural glass and low-power mobile electronic applications, wavelength-selective TPV offer a promising route to inexpensive, widespread solar adoption on small and large surfaces that were previously inaccessible.

Data availability. The data is available from the corresponding author upon reasonable request.

Received: 21 December 2016; Accepted: 6 September 2017;

References

1. Denholm, P. & Margolis, R. M. Land-use requirements and the per-capita solar footprint for photovoltaic generation in the United States. *Energy Policy* **36**, 3531–3543 (2008).
2. Moriarty, P. & Honnery, D. What is the global potential for renewable energy? *Renew. Sustain. Energy Rev.* **16**, 244–252 (2012).
3. *A Snapshot of Global PV (1992–2014)* (Photovoltaic Power Systems Programme, International Energy Agency, 2014); http://www.iea-pvps.org/fileadmin/dam/public/report/technical/PVPS_report__A_Snapshot_of_Global_PV_-_1992-2014.pdf
4. Jelle, B. Building integrated photovoltaics: a concise description of the current state of the art and possible research pathways. *Energies* **9**, 21 (2016).
5. Eiffert, P. & Kiss, G. J. *Building-Integrated Photovoltaic Designs for Commercial and Institutional Structures: A Sourcebook for Architects* Report no. NREL/BK-520-25272 (National Renewable Energy Laboratory, Golden, CO, 2000).
6. Gagnon, P. et al. *Rooftop Solar Photovoltaic Technical Potential in the United States* Report no. NREL/PR 6A20 65586 (National Renewable Energy Laboratory, 2016).
7. *Commercial Buildings Energy Consumption Survey (CBECS) Data* (US Energy Information Administration, 2012); http://www.eia.gov/consumption/commercial/data/2012/
8. *2009 Residential Energy Consumption Survey (RECS) Data* (US Energy Information Admnistration, 2009); http://www.eia.gov/consumption/residential/data/2009/index.php?view=characteristics
9. Yang, R. J. & Zou, P. X. W. Building integrated photovoltaics (BIPV): costs, benefits, risks, barriers and improvement strategy. *Int. J. Const. Manage* **16**, 39–53 (2016).
10. Lunt, R. R. Theoretical limits for visibly transparent photovoltaics. *Appl. Phys. Lett.* **101**, 043902 (2012). **This work provides the calculation of the theoretical efficiency limits for TPV as a function of AVT.**

11. Lunt, R. R. et al. Practical roadmap and limits to nanostructured photovoltaics. *Adv. Mater.* **23**, 5712–5727 (2011).
12. Yoon, J. et al. Ultrathin silicon solar microcells for semitransparent, mechanically flexible and microconcentrator module designs. *Nat. Mater.* **7**, 907–915 (2008).
13. Eperon, G. E. et al. Efficient, semitransparent neutral-colored solar cells based on microstructured formamidinium lead trihalide perovskite. *J. Phys. Chem. Lett.* **6**, 129–138 (2015).
14. Eperon, G. E., Burlakov, V. M., Goriely, A. & Snaith, H. J. Neutral color semitransparent microstructured perovskite solar cells. *ACS Nano* **8**, 591–598 (2014).
15. Leijtens, T. et al. Stability of metal halide perovskite solar cells. *Adv. Energy Mater.* **5**, 1500963 (2015).
16. Zhang, X., Eperon, G. E., Liu, J. & Johansson, E. M. J. Semitransparent quantum dot solar cell. *Nano Energy* **22**, 70–78 (2016).
17. Saifullah, M. et al. Development of semitransparent CIGS thin-film solar cells modified with a sulfurized-AgGa layer for building applications. *J. Mater. Chem. A* **4**, 10542–10551 (2016).
18. Karsthof, R., Räcke, P., von Wenckstern, H. & Grundmann, M. Semi-transparent NiO/ZnO UV photovoltaic cells. *Phys. Status Solidi A* **213**, 30–37 (2016).
19. Lim, J. W., Lee, D. J. & Yun, S. J. Semi-transparent amorphous silicon solar cells using a thin p-si layer and a buffer layer. *ECS Solid State Lett.* **2**, Q47–Q49 (2013).
20. Guo, F. et al. High-performance semitransparent perovskite solar cells with solution-processed silver nanowires as top electrodes. *Nanoscale* **7**, 1642–1649 (2015).
21. Della Gaspera, E. et al. Ultra-thin high efficiency semitransparent perovskite solar cells. *Nano Energy* **13**, 249–257 (2015).
22. Meiss, J. et al. Near-infrared absorbing semitransparent organic solar cells. *Appl. Phys. Lett.* **99**, 193307 (2011).
23. Lee, J.-Y., Connor, S. T., Cui, Y. & Peumans, P. Semitransparent organic photovoltaic cells with laminated top electrode. *Nano Lett.* **10**, 1276–1279 (2010).
24. Betancur, R. et al. Transparent polymer solar cells employing a layered light-trapping architecture. *Nat. Photon.* **7**, 995–1000 (2013).
25. Adikaari, A. A. D. et al. Near infrared up-conversion in organic photovoltaic devices using an efficient Yb^{3+}:Ho^{3+} Co-doped Ln$_2$BaZnO$_5$ (Ln = Y, Gd) phosphor. *J. Appl. Phys.* **111**, 094502 (2012).
26. Zhang, K. et al. High-performance, transparent, dye-sensitized solar cells for see-through photovoltaic windows. *Adv. Energy Mater.* **4**, 1301966 (2014).
27. Chiang, Y.-F. et al. Non-color distortion for visible light transmitted tandem solid state dye-sensitized solar cells. *Renew. Energy* **59**, 136–140 (2013).
28. Meiss, J. et al. Highly efficient semitransparent tandem organic solar cells with complementary absorber materials. *Appl. Phys. Lett.* **99**, 043301 (2011).
29. Yusoff, A. Rb. M. et al. High-performance semitransparent tandem solar cell of 8.02% conversion efficiency with solution-processed graphene mesh and laminated ag nanowire top electrodes. *Adv. Energy Mater.* **4**, 1301989 (2014).
30. Lee, K.-T. et al. Colored dual-functional photovoltaic cells. *J. Optics* **18**, 064003 (2016).
31. Lunt, R. R. & Bulovic, V. Transparent, near-infrared organic photovoltaic solar cells for window and energy-scavenging applications. *Appl. Phys. Lett.* **98**, 113305 (2011). **This work demonstrates the approach to wavelength-selective TPV with high AVT.**
32. Chen, C.-C. et al. Visibly transparent polymer solar cells produced by solution processing. *ACS Nano* **6**, 7185–7190 (2012). **This study utilizes the polymer PBDTT-DPP to fabricate fully solution-processed high efficiency wavelength-selective TPV.**
33. Liu, F. et al. Efficient semitransparent solar cells with high NIR responsiveness enabled by a small-bandgap electron acceptor. *Adv. Mater.* **29**, 1606574 (2017).
34. Wang, W. et al. Fused hexacyclic nonfullerene acceptor with strong near-infrared absorption for semitransparent organic solar cells with 9.77% efficiency. *Adv. Mater.* **29**, 1701308 (2017). In this work, wavelength-selective photoactive materials are utilized to fabricate TPV with up to 9.77% PCE and 32% AVT.
35. Batchelder, J. S., Zewai, A. H. & Cole, T. Luminescent solar concentrators. 1: Theory of operation and techniques for performance evaluation. *Appl. Opt.* **18**, 3090–3110 (1979).
36. Yang, C. & Lunt, R. R. Limits of visibly transparent luminescent solar concentrators. *Adv. Opt. Mater.* **5**, 1600851 (2017). **This work calculates the theoretical performance limits of UV/NIR wavelength-selective LSCs and identifies key materials and engineering challenges to enable complete optimization and commercial deployment.**
37. Slooff, L. H. et al. A luminescent solar concentrator with 7.1% power conversion efficiency. *Phys. Status Solidi R* **2**, 257–259 (2008).
38. Meinardi, F. et al. Highly efficient large-area colourless luminescent solar concentrators using heavy-metal-free colloidal quantum dots. *Nat. Nanotech* **10**, 878–885 (2015).
39. Meinardi, F. et al. Highly efficient luminescent solar concentrators based on earth-abundant indirect-bandgap silicon quantum dots. *Nat. Photon.* **11**, 177–185 (2017).
40. Chen, R.-T., Chau, J. L. H. & Hwang, G.-L. Design and fabrication of diffusive solar cell window. *Renew. Energy* **40**, 24–28 (2012).
41. Zhao, Y. & Lunt, R. R. Transparent luminescent solar concentrators for large-area solar windows enabled by massive Stokes-shift nanocluster phosphors. *Adv. Energy Mater.* **3**, 1143–1148 (2013). **UV-selective hexanuclear metal halide nanoclusters are utilized to demonstrate visibly clear LSCs, scalable to practical sizes due to a large Stokes shift, which significantly reduces reabsorption losses.**
42. Zhao, Y., Meek, G. A., Levine, B. G. & Lunt, R. R. Near-infrared harvesting transparent luminescent solar concentrators. *Adv. Opt. Mater.* **2**, 606–611 (2014). **Organic salts are utilized to demonstrate the approach of NIR wavelength-selective LSCs with high AVT and CRI of 88% and 94, respectively.**
43. Banal, J. L. et al. A transparent planar concentrator using aggregates of gem-pyrene ethenes. *Adv. Energy Mater.* **5**, 1500818 (2015).
44. Erickson, C. S. et al. Zero-reabsorption doped-nanocrystal luminescent solar concentrators. *ACS Nano* **8**, 3461–3467 (2014). **UV-selective LSCs utilizing Mn-doped ZnSe quantum dots with a large Stokes shift are demonstrated, expanding the catalogue of non-toxic luminescent materials applicable to wavelength-selective LSCs scalable to practical sizes.**
45. Rondão, R. et al. High-performance near-infrared luminescent solar concentrators. *ACS Appl. Mater. Interfac.* **9**, 12540–12546 (2017).
46. Ostroverkhova, O. Organic optoelectronic materials: mechanisms and applications. *Chem. Rev.* **116**, 13279–13412 (2016).
47. Schlenker, C. W. & Thompson, M. E. in *Unimolecular and Supramolecular Electronics I* 1st edn, Vol. 312 (ed Metzger, R. M.) Ch. 4 (Springer Verlag, Berlin, 2011).
48. Lunt, R. R. et al. Exciton diffusion lengths of organic semiconductor thin films measured by spectrally resolved photoluminescence quenching. *J. Appl. Phys.* **105**, 053711 (2009).
49. Wu, M.-Y., Jacobberger, R. M. & Arnold, M. S. Design length scales for carbon nanotube photoabsorber based photovoltaic materials and devices. *J. Appl. Phys.* **113**, 204504 (2013).
50. Peumans, P., Soichi, U. & Forrest, S. R. Efficient bulk heterojunction photovoltaic cells using small-molecular-weight organic thin films. *Nature* **425**, 158–162 (2003).
51. Inganäs, O., Tang, Z., Bergqvist, J. & Tvingstedt, K. in *Organic Solar Cells: Fundamentals, Devices, and Upscaling* 1st edn, Vol. 1 (eds Rand, B. P. & Richter, H.) Ch. 8 (CRC Press, Boca Raton, FL, 2014).
52. Menke, S. M., Luhman, W. A. & Holmes, R. J. Tailored exciton diffusion in organic photovoltaic cells for enhanced power conversion efficiency. *Nat. Mater.* **12**, 152–157 (2013).
53. Mullenbach, T. K. et al. Connecting molecular structure and exciton diffusion length in rubrene derivatives. *Adv. Mater.* **25**, 3689–3693 (2013).
54. Lunt, R. R., Benziger, J. B. & Forrest, S. R. Relationship between crystalline order and exciton diffusion length in molecular organic semiconductors. *Adv. Mater.* **22**, 1233–1236 (2010).
55. Choi, S., Potscavage, W. J. Jr & Kippelen, B. Area-scaling of organic solar cells. *J. Appl. Phys.* **106**, 054507 (2009).
56. Cho, D.-Y. et al. Transparent and flexible amorphous InZnAlO films grown by roll-to-roll sputtering for acidic buffer-free flexible organic solar cells. *Org. Electron.* **24**, 227–233 (2015).
57. Jean, J., Wang, A. & Bulović, V. In situ vapor-deposited parylene substrates for ultra-thin, lightweight organic solar cells. *Org. Electron.* **31**, 120–126 (2016).
58. Choi, K.-H., Jeong, J.-A. & Kim, H.-K. Dependence of electrical, optical, and structural properties on the thickness of IZTO thin films grown by linear facing target sputtering for organic solar cells. *Sol. Energy Mater. Sol. Cells* **94**, 1822–1830 (2010).
59. Choi, Y.-Y., Kang, S. J. & Kim, H.-K. Rapid thermal annealing effect on the characteristics of ZnSnO$_3$ films prepared by RF magnetron sputtering. *Curr. Appl. Phys.* **12** (Suppl. 4), S104–S107 (2012).
60. Lee, H.-M., Kang, S.-B., Chung, K.-B. & Kim, H.-K. Transparent and flexible amorphous In-Si-O films for flexible organic solar cells. *Appl. Phys. Lett.* **102**, 021914 (2013).
61. Smith, S. & Chen, W.-H. in *Design for Innovative Value Towards a Sustainable Society* 1st edn, Vol. 1 (eds Matsumoto, M. *et al.*) Ch. 150 (Springer, 2012).
62. Weiser, A., Lang, D. J., Schomerus, T. & Stamp, A. Understanding the modes of use and availability of critical metals – An expert-based scenario analysis for the case of indium. *J. Clean. Prod.* **94**, 376–393 (2015).

63. Hu, L., Wu, H. & Cui, Y. Metal nanogrids, nanowires, and nanofibers for transparent electrodes. *MRS Bull.* **36**, 760–765 (2011).
64. Li, H. et al. Doctor-blade deposition of quantum dots onto standard window glass for low-loss large-area luminescent solar concentrators. *Nat. Energy* **1**, 16157 (2016).
65. Bernardi, M. et al. Solar energy generation in three dimensions. *Energy Environ. Sci.* **5**, 6880–6884 (2012).
66. Marion, W. & Wilcox, S. *Users Manual for TMY3 Data Sets* (National Renewable Energy Laboratory, 2008); http://www.nrel.gov/docs/fy08osti/43156.pdf
67. Marion, W. & Wilcox, S. *Solar Radiation Data Manual for Buildings* (National Renewable Energy Laboratory, 1995); http://www.nrel.gov/docs/legosti/old/7904.pdf
68. Young, M. et al. Angle dependence of transparent photovoltaics in conventional and optically inverted configurations. *Appl. Phys. Lett.* **103**, 133304 (2013).
69. Ding, Y. et al. Influence of photovoltaic angle-dependence on overall power output for fixed building integrated configurations. *Sol. Energy Mater. Sol. Cells* **132**, 523–527 (2015).
70. Ball, J. M. et al. Optical properties and limiting photocurrent of thin-film perovskite solar cells. *Energy Environ. Sci.* **8**, 602–609 (2015).
71. Leem, J. W., Guan, X.-Y. & Yu, J. S. Tunable distributed Bragg reflectors with wide-angle and broadband high-reflectivity using nanoporous/dense titanium dioxide film stacks for visible wavelength applications. *Opt. Express* **22**, 18519–18526 (2014).
72. Espinosa, N., Hosel, M., Angmo, D. & Krebs, F. C. Solar cells with one-day energy payback for the factories of the future. *Energy Environ. Sci.* **5**, 5117–5132 (2012).
73. Rosch, R. et al. Investigation of the degradation mechanisms of a variety of organic photovoltaic devices by combination of imaging techniques: the ISOS-3 inter-laboratory collaboration. *Energy Environ. Sci.* **5**, 6521–6540 (2012).
74. Mateker, W. R. et al. Minimal long-term intrinsic degradation observed in a polymer solar cell illuminated in an oxygen-free environment. *Chem. Mater.* **27**, 404–407 (2015).
75. Roesch, R. et al. Polymer solar cells with enhanced lifetime by improved electrode stability and sealing. *Sol. Energy Mater. Sol. Cells* **117**, 59–66 (2013).
76. Burlingame, Q. et al. Reliability of small molecule organic photovoltaics with electron-filtering compound buffer layers. *Adv. Energy Mater.* **6**, 1601094 (2016).
77. Gevorgyan, S. A. et al. Lifetime of organic photovoltaics: status and predictions. *Adv. Energy Mater.* **6**, 1501208 (2016).
78. Lungenschmied, C. et al. Flexible encapsulation for organic solar cells. *Proc. SPIE* **6197**, 619712 (2006).
79. Chen, C.-C. et al. High-performance semi-transparent polymer solar cells possessing tandem structures. *Energy Environ. Sci.* **6**, 2714–2720 (2013).
80. Young, M. et al. Organic heptamethine salts for photovoltaics and detectors with near-infrared photoresponse up to 1600 nm. *Adv. Opt. Mater.* **4**, 1028–1033 (2016).
81. Zhang, H. et al. Semitransparent organic photovoltaics using a near-infrared absorbing cyanine dye. *Sol. Energy Mater. Sol. Cells* **118**, 157–164 (2013).
82. Suddard-Bangsund, J. et al. Organic salts as a route to energy level control in low bandgap, high open-circuit voltage organic and transparent solar cells that approach the excitonic voltage limit. *Adv. Energy Mater.* **6**, 1501659 (2015).
83. Knupfer, M. Exciton binding energies in organic semiconductors. *Appl. Phys. A* **77**, 623–626 (2003).
84. Kraner, S., Scholz, R., Koerner, C. & Leo, K. Design proposals for organic materials exhibiting a low exciton binding energy. *J. Phys. Chem. C* **119**, 22820–22825 (2015).
85. Zimmerman, J. D. et al. Porphyrin-tape/C60 organic photodetectors with 6.5% external quantum efficiency in the near infrared. *Adv. Mater.* **22**, 2780–2783 (2010).
86. Finlayson, E. U. *et al. WINDOW 4.0: Documentation of Calculation Procedures* Report no. LBL-33943 (Lawrence Berkeley Laboratory and Enermodal Engineering, Inc., 1993).
87. Berson, D. M., Dunn, F. A. & Takao, M. Phototransduction by retinal ganglion cells that set the circadian clock. *Science* **295**, 1070–1073 (2002).
88. Burkhard, G. F., Hoke, E. T. & McGehee, M. D. Accounting for interference, scattering, and electrode absorption to make accurate internal quantum efficiency measurements in organic and other thin solar cells. *Adv. Mater.* **22**, 3293–3297 (2010).
89. Pandey, R. & Holmes, R. J. Characterizing the charge collection efficiency in bulk heterojunction organic photovoltaic cells. *Appl. Phys. Lett.* **100**, 083303 (2012).
90. Treml, B. E. & Hanrath, T. Quantitative framework for evaluating semitransparent photovoltaic windows. *ACS Energy Lett.* **1**, 391–394 (2016).
91. Davy, N. C. et al. Pairing of near-ultraviolet solar cells with electrochromic windows for smart management of the solar spectrum. *Nat. Energy* **2**, 17104 (2017). **UV-selective TPV are demonstrated to directly power electrochromic smart windows to reduce lighting, heating, and cooling costs in buildings.**
92. Llordes, A. et al. Linear topology in amorphous metal oxide electrochromic networks obtained via low-temperature solution processing. *Nat. Mater.* **15**, 1267–1273 (2016).
93. Llordes, A., Garcia, G., Gazquez, J. & Milliron, D. J. Tunable near-infrared and visible-light transmittance in nanocrystal-in-glass composites. *Nature* **500**, 323–326 (2013).
94. *Ubiquitous Energy's Truly Transparent Solar Technology Demonstrated Globally in BMW Brand Stores* (Ubiquitous Energy, 2016); http://ubiquitous.energy/bmw_iexhibition
95. Baker, D. R. Elon Musk's solar roof is pretty, but it's not the first. *San Francisco Chronicle* (31 October 2016); http://www.sfchronicle.com/business/article/Elon-Musk-s-solar-roof-isn-t-the-first-10418690.php
96. *Windows for High Performance Commercial Buildings* (2015); http://www.commercialwindows.org/vt.php
97. Fisette, P. *Windows: Understanding Energy Efficient Performance* (University of Massachusetts, 2003); https://bct.eco.umass.edu/publications/articles/windows-understanding-energy-efficient-performance/
98. Mescher, J. et al. Design rules for semi-transparent organic tandem solar cells for window integration. *Org. Electron.* **15**, 1476–1480 (2014).
99. Alessi, P. J. *et al. Colorimetry* Report No. 15:2004 (International Commission on Illumination, 2004).
100. Franklin, E., Everett, V., Blakers, A. & Weber, K. Sliver solar cells: high-efficiency, low-cost PV technology. *Adv. Optoelectron.* **2007**, 9 (2007).
101. Bu, L. et al. Semitransparent fully air processed perovskite solar cells. *ACS Appl. Mater. Interf.* **7**, 17776–17781 (2015).
102. Debije, M. G. & Verbunt, P. P. C. Thirty years of luminescent solar concentrator research: solar energy for the built environment. *Adv. Energy Mater.* **2**, 12–35 (2012).
103. Tu, X., Manohar, S., Jagota, A. & Zheng, M. DNA sequence motifs for structure-specific recognition and separation of carbon nanotubes. *Nature* **460**, 250–253 (2009).

Acknowledgements

Financial support for this work was provided by the National Science Foundation (CBET-1511098, 1254662, and 1702591, to C.J.T. and R.R.L.) and by the American Physical Society through the Stanford R. Ovshinsky Sustainable Energy Fellowship Award (R.R.L.). C.J.T. also acknowledges the Department of Education for support under the Graduate Assistantship in Areas of National Need (GAANN) Award (P200A140215). The authors thank G. Flores for assistance with the survey of transparent photovoltaic demonstrations and D. Hess for reviewing the manuscript.

Competing interests

R.P., M.C.B., and R.R.L. have minority ownership interest in Ubiquitous Energy. M.C.B. is the current CEO of Ubiquitous Energy. All other authors declare no competing financial interests.

Additional information

Supplementary information is available for this paper at https://doi.org/10.1038/s41560-017-0016-9.

Reprints and permissions information is available at www.nature.com/reprints.

Correspondence and requests for materials should be addressed to R.R.L.